AGU PUBLICATIONS

JGR

Journal of Geophysical Research: Oceans

RESEARCH ARTICLE

10.1002/2017JC012773

Shelf Circulation Induced by an Orographic Wind Jet

Laura Ràfols[1,2], Manel Grifoll[1], Gabriel Jordà[3], Manuel Espino[1], Abdel Sairouní[2], and Manel Bravo[2]

[1]Maritime Engineering Laboratory (LIM-UPC), Technical University of Catalonia (BarcelonaTech), Barcelona, Spain, [2]Meteorological Service of Catalonia (SMC), Barcelona, Spain, [3]Mediterranean Institute for Advanced Studies (UIB-CSIC), Esporles, Spain

Key Points:
- The shelf circulation induced by cross-shelf wind jets is investigated using the ROMS model and data measurements from buoys and a HF radar
- The results show a sea level set-down near the coastline and a two-layer circulation in the cross-shelf direction
- The cross-shelf momentum balance during a wind-jet event shows different balancing terms at shallow and deep regions

Correspondence to:
L. Ràfols,
laura.rafols@upc.edu

Citation:
Ràfols, L., Grifoll, M., Jordà, G., Espino, M., Sairouní, A., & Bravo, M. (2017). Shelf circulation induced by an orographic wind jet. *Journal of Geophysical Research: Oceans*, *122*. https://doi.org/10.1002/2017JC012773

Received 9 FEB 2017
Accepted 27 SEP 2017
Accepted article online 30 SEP 2017

Abstract The dynamical response to cross-shelf wind-jet episodes is investigated. The study area is located at the northern margin of the Ebro Shelf, in the Northwestern (NW) Mediterranean Sea, where episodes of strong northwesterly wind occur. In this case, the wind is channeled through the Ebro Valley and intensifies upon reaching the sea, resulting in a wind jet. The wind-jet response in terms of water circulation and vertical density structure is investigated using a numerical model. The numerical outputs agree with water current observations from a high-frequency radar. Additionally, temperature, sea level, and wind measurements are also used for the skill assessment of the model. For the wind-jet episodes, the numerical results show a well-defined two-layer circulation in the cross-shelf direction, with the surface currents in the direction of the wind. This pattern is consistent with sea level set-down due to the wind effect. The comparison of the vertical structure response for different episodes revealed that the increase of stratification leads to an onshore displacement of the transition from inner shelf to mid-shelf. In general, the cross-shelf momentum balance during a wind-jet episode exhibits a balance between the frictional terms and the pressure gradient in shallow waters, shifting to a balance between the Coriolis force and the wind stress terms in deeper waters.

1. Introduction

Wind-driven shelf circulation investigations have focused their attention on the effects of along-shelf winds, which result in upwelling or downwelling. However, cross-shelf circulation due to cross-shelf winds is larger than cross-shelf circulation due to along-shelf winds of the same magnitude in water depths that are less than the surface boundary layer (SBL) thickness (Lentz & Fewings, 2012). In this region, cross-shelf winds can generate substantial cross-shelf transport and, therefore, upwelling and downwelling (Tilburg, 2003).

The continental shelf is constrained by the surfzone and the continental slope and can be divided in three dynamically different regions. Going from shallower to deeper waters, there is the inner shelf, the mid-shelf, and the outer-shelf. Thus, the inner shelf is a transition zone (from surfzone to mid-shelf) that extends water depths up to tens of meters. Since the surfzone dynamics are dominated by breaking waves and the mid-shelf is usually in geostrophic balance, the inner shelf may have elements of both (Fewings & Lentz, 2010). In this sense, previous investigations (collected in Lentz & Fewings, 2012) have analyzed the cross-shelf circulation response due to cross-shelf winds and found two dynamical regions: onshore (inner shelf) and offshore (mid-shelf) of the location where the SBL intersects the bottom. Those studies also established that during cross-shelf winds, the cross-shelf circulation is confined to the SBL. Thus, in this work, since it is focused on the shelf circulation due to cross-shelf winds, the SBL is defined as the depth at which the cross-shelf circulation in the upper layer shuts off and the inner shelf is defined as the region onshore of where the SBL intersects the bottom (similarly to Tilburg, 2003 and Horwitz & Lentz, 2014, when analyzing the response to a cross-shelf wind stress).

Regions with coastal wind jets induced by orographic effects are areas with complex dynamics in terms of water circulation response (Grifoll et al., 2015; Jordà, 2005; Trasviña et al., 1995), spatial and temporal wind variability (Jiang et al., 2009), and sharp wave height variations (Shimada & Kawamura, 2006). In this sense, several researchers have focused on the description of different aspects such as the wave generation/decaying process (Shimada & Kawamura, 2006), the surface water cooling effect due to upwelling (Trasviña et al., 1995), or the influence of the sea surface roughness variation due to the wave climate (Grifoll et al., 2016b).

However, these regions have still not been thoroughly investigated and some aspects of the water circulation response to wind jets remain unclear. Thus, regions where the circulation pattern may be rapidly modified under the presence of a wind jet deserve special attention. Grifoll et al. (2015) performed an observational study and found a seasonal response of the water circulation due to cross-shelf winds. They also highlighted the presence of cold water at the surface and attempted to discern between an upwelling process and a cooling effect due to mixing. However, the common sparsity of their measurements does not allow one to extrapolate their conclusions to the whole region since the shelf response to cross-shelf winds is highly dependent on water depth. Tilburg (2003) showed that at the inner shelf, cross-shelf winds can result in cross-shelf velocities in the top few meters of the water column that are similar in magnitude to those generated by along-shelf winds. In fact, the author found that cross-shelf winds can be the primary mechanism for cross-shelf transport within the friction-dominated inner shelf. Horwitz and Lentz (2014) noted that it is the cross-shelf rather than vertical density gradient that is critical to predict transport driven by a cross-shelf wind stress. To investigate these processes, the use of numerical modeling has been proven to be a powerful tool (e.g., Grifoll et al., 2016b; Horwitz & Lentz, 2014; Tilburg, 2003).

At the north Ebro Shelf (NES) in the NW Mediterranean Sea (see Figure 1), when the wind approaches from the NW, channeled through the Ebro Valley, it results in an intensified wind upon reaching the sea, commonly known as an orographic wind jet. This wind is dry, cold, perpendicular to the coastline (cross-shelf wind), and associated with high wind intensities. The synoptic situation that causes this wind jet is related to a high-pressure area over the Bay of Biscay and a low-pressure area in the western Mediterranean Sea (Riosalido et al., 1986). The wind jet is more common and intense in autumn and winter, when a larger atmospheric pressure gradient exists, but a small pressure difference along the Ebro Valley is enough to initiate wind during any season (Riosalido et al., 1986). In addition, cross-shelf winds can have a significant

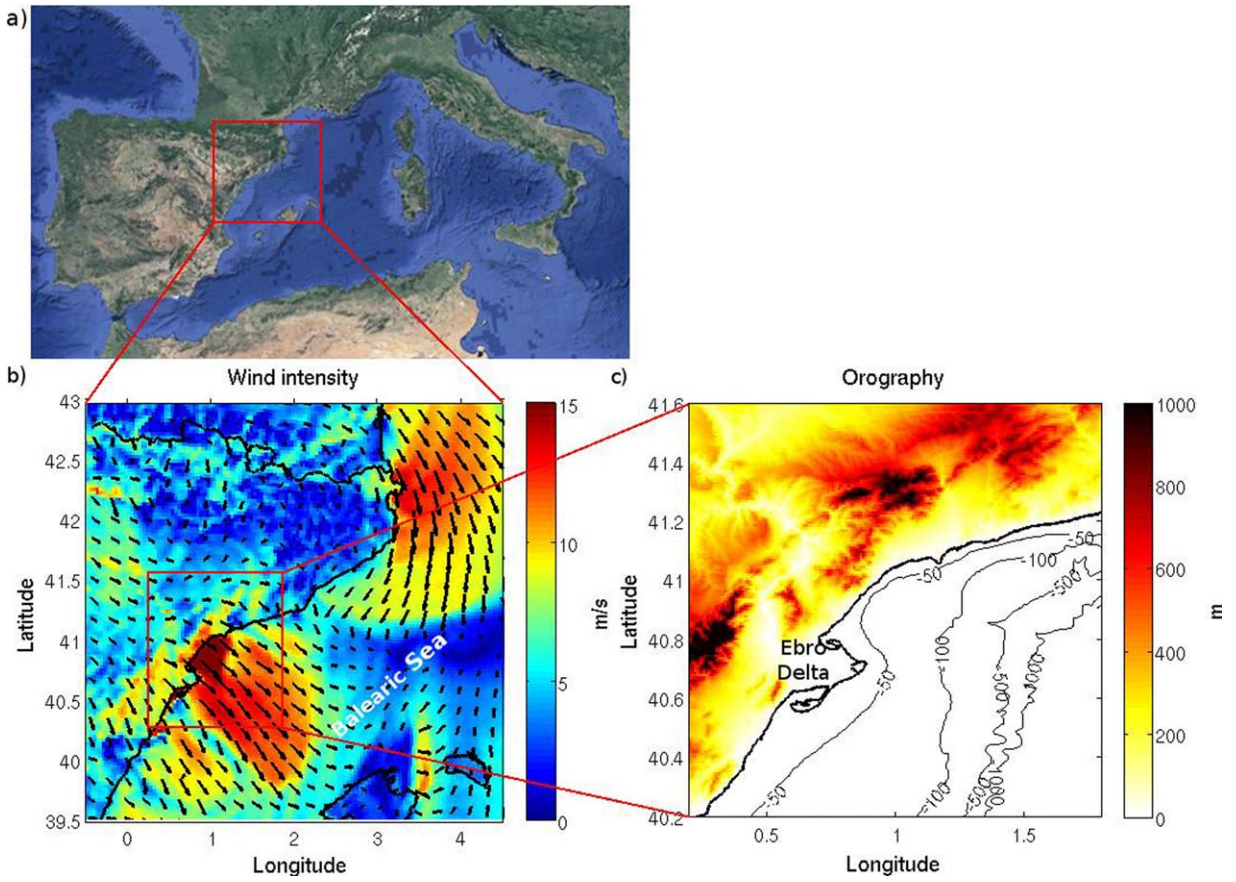

Figure 1. (a) NW Mediterranean Sea (map data from Google, TerraMetrics). (b) Example of a NW wind-jet event (figure created with the same wind data used in this study). (c) Ebro Delta orography and isobaths.

contribution to cross-shelf transport of water and material on the continental shelf (Tilburg, 2003), with further implications to suspended matter and biological processes.

The main goal of this study is to describe the effects of a wind jet on the circulation and hydrographic properties of the continental shelf. To do that, a numerical model has been implemented in the NES and run for a period of 6 months (from 1 March 2014 to 1 September 2014). This period was selected due to the high availability of different types of observational data, which has allowed for the skill assessment of the numerical model results. The influence of the stratification at the initial stages of the wind-jet episodes and the main mechanisms that govern the cross-shelf circulation during those episodes are investigated.

This work is organized as follows. In section 2, an overview of the main characteristics of the study area, a description of the numerical model implementation, and an exposition of the observational data available at the zone, which is used to validate the model, are presented. Section 3 contains the results. First, the wind data are analyzed to locate and characterize the wind-jet events, then the numerical model is validated using data from an HF radar and finally a selected wind-jet episode is analyzed in detail, while a more general description is compiled for the remaining set of events. Section 4 contains a discussion, where the results are compared with previous studies focusing on the role of the stratification and the estimation of the momentum balance terms. Finally, the most relevant conclusions are summarized in section 5.

2. Data and Methodology

2.1. Study Area

The NES is located at the southern part of the Catalan coast, between latitudes 40.4°N and 41.1°N and longitudes 0.4°E and 1.3°E (see Figure 1). This area includes the Ebro Delta shelf, which is characterized by the transition from a narrow shelf (∼10 km) at its northern end to a broader shelf (∼60 km) toward the south. The shelf break is at approximately 160 m water depth.

The regional topography (see Figure 1c), with the coastal mountain chain breached by the Ebro River valley, exerts a significant control on the wind climate (Bolaños et al., 2009). The most characteristic wind of the region is the northwesterly wind (Mistral), which often results in a cross-shelf wind jet. Figure 1b shows an example of a NW wind-jet event. An intensification of the mean conditions occurs at the northern margin of the Ebro Delta, delimitating the wind-jet area. Grifoll et al. (2015) analyzed the percentage of time that NW wind blows for each month: during winter this percentage reaches 80%, decreasing significantly during summer (less than 20%).

The Mediterranean Sea is a microtidal environment where the astronomical tide is very small and the sea level variation is not as important as in other seas. At the Ebro Delta, the maximum range of the astronomical tide is 0.25 m, while the sea level variations caused by storm surges have a range of 1 m (Bolaños et al., 2009).

The predominant current in the Balearic Sea is the quasi-permanent current known as the Northern Current, which is an entity flowing along the continental slope (Millot, 1999). This current can be modified by mesoscale events such as current meandering or eddies (Font et al., 1995). In winter, the Northern Current becomes deeper and narrower. At this time, it tends to flow closer to the slope and develops relatively intense mesoscale meanders (Flexas et al., 2002; Millot, 1999). The mean current intensity is not very strong (∼10 cm/s at 100 m depth) but it shows a seasonal intensification in winter when velocities can reach higher values (∼40 cm/s at 100 m depth) (Bolaños et al., 2009).

At the Ebro Delta, the widening of the continental shelf produces a gyre of almost 90° in the direction of the isobaths, becoming a barrier to the SW circulation of the Northern Current, which is deviated to the south. Some studies have examined the likely presence of an anticyclonic circulation pattern controlled by the bathymetry in the zone (Espino et al., 1998; Font, 1986). Using 1 year water velocity observations measured at 43.5 m, Grifoll et al. (2015) showed that the mean flow was polarized following the isobaths at the shelf region; however, significant seaward near-surface velocities occurred predominantly during offshore wind events.

The river discharge off the Ebro Delta may have a relevant influence in the circulation pattern of the area. The freshwater enters the sea flowing to the NE but is deviated by the SW circulation to the E and then to

the S, due to the Coriolis force (Durand et al., 2002). This mesoscale event of the confrontation of flows with different salinity (and therefore different density) can produce anticyclonic circulation (Font, 1986). Nevertheless, Durand et al. (2002) and Mestres et al. (2003) showed that the effects of the river plume on the circulation are only important near the river mouth (∼10 km offshore).

2.2. Numerical Model

The Regional Ocean Modeling System (ROMS) is used in this study. It is a split-explicit, free-surface, terrain-following, primitive equations oceanic model that solves the 3-D Reynolds-averaged Navier-Stokes equations using the hydrostatic and Boussinesq assumptions (Haidvogel et al., 2008; Shchepetkin & McWilliams, 2005). The model uses finite-difference approximations on a terrain-following vertical coordinate (sigma-coordinate) and on a horizontal curvilinear Arakawa C grid.

A high-resolution domain is implemented at the NES. It has 20 vertical sigma levels and a horizontal grid of 260 × 166 points with a resolution of 350 m in both directions that covers an area of 91 × 58.1 km (see Figure 2b). The model implementation includes a Generic Length-Scale turbulent vertical mixing scheme with the $k-\epsilon$ parametrization, a logarithmic profile for the bottom boundary layer with a bottom roughness of 0.005 m, and horizontal mixing terms in geopotential surfaces.

As initial and boundary conditions, data from IBI-MFC (Iberian Biscay Irish - Monitoring and Forecasting Centre) product are used. This product (http://marine.copernicus.eu) includes all main forcings (i.e., tidal forcing, high-frequency atmospheric forcing, freshwater river discharge, etc.) and is based on a (eddy-resolving) NEMO model application run at 1/36° horizontal resolution. The outputs provided by the IBI-MFC used in our numerical model are 3-D daily means of fields of temperature, salinity, sea surface height, zonal velocity, and meridional velocity and hourly means of surface fields (sea surface height and barotropic currents).

For atmospheric forcing, the outputs from the Weather Research and Forecasting (WRF, Skamarock et al., 2008) model implemented at high resolution (3 km) at the Meteorological Service of Catalonia (SMC; http://www.meteo.cat) are used. Specifically, the wind velocity, the atmospheric pressure, humidity and temperature, the longwave and shortwave radiation, and the rainfall rate are used. Moreover, the turbulent heat fluxes (latent and sensible) are derived from the atmospheric parameters using the bulk parametrization of Fairall et al. (1996).

Finally, the Ebro River discharge is characterized by using data from the Automatic Hydrologic Information System of the Ebro River basin (owned by the Confederación Hidrográfica del Ebro), which has a network of measurement and remote control instruments that transmits and processes data periodically. The data used to force the numerical model consist of daily measurements of river runoff and temperature.

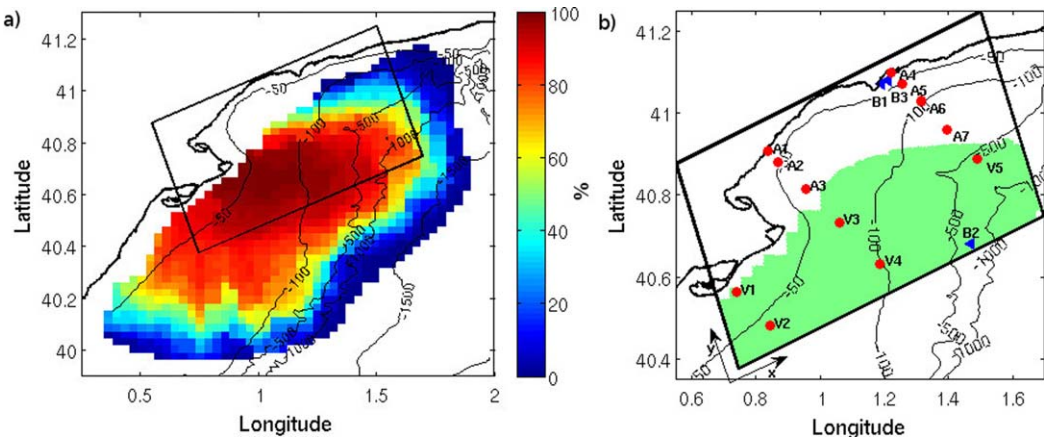

Figure 2. (a) HF radar data availability for the studied period. The black rectangle specifies the model domain. (b) Resultant validation area and validation points' locations. The black rectangle is the numerical model domain; the tide gauge (B1), the deep water buoy (B2), and the coastal wave buoy (B3) are represented with blue triangles. The red dots are the points chosen for validation and analysis in the results and discussion sections. The "V" points mark where the results can be validated with HF radar data. The green area shows where more than 50% of the HF radar data are available. The figure also includes the reference *x*/*y* axis used.

The points where the model results are validated and analyzed (see Figure 2b) are selected according to the wind intensification zone (Figure 1b). Points A1, A2, A3, V3, and V4 correspond to a cross-section where the mean wind velocities are higher (wind-jet axis). Seven additional points correspond to two parallel cross-sections of the previous one which are located "outside" the wind-jet axis (V1, V2 along the west of the wind-jet axis and A4, A5, A6, A7, and V5 along the east of it).

2.3. Validation Techniques

In order to assess the model behavior, the estimation of the bias, the Root Mean Square Deviation (RMSD), the Pearson's correlation (Pearson's *r*), and the model skill score (*d*, following the method presented in Willmott, 1981) are undertaken. These values are defined as follows:

$$bias = \frac{1}{N}\sum X_{model} - X_{obs} \tag{1}$$

$$RMSD = \sqrt{\frac{1}{N}\sum \left(X_{model} - X_{obs}\right)^2} \tag{2}$$

$$r = \frac{\sum \left(\left(X_{model} - \overline{X_{model}}\right)\left(X_{obs} - \overline{X_{obs}}\right)\right)}{\sqrt{\sum \left(X_{model} - \overline{X_{model}}\right)^2}\sqrt{\sum \left(X_{obs} - \overline{X_{obs}}\right)^2}} \tag{3}$$

$$d = 1 - \frac{\sum \left|X_{model} - X_{obs}\right|^2}{\sum \left(\left|X_{model} - \overline{X_{obs}}\right| + \left|X_{obs} - \overline{X_{obs}}\right|\right)^2} \tag{4}$$

where N is the number of samples. Pearson's r describes consistent proportional increases or decreases about respective means of the two quantities, but it makes too few distinctions among the type or magnitudes of possible covariations (Willmott, 1981). By contrast, d is not a measure of correlation or association in the formal sense but rather a measure of the degree to which a model's predictions are error free. Unlike r, d is sensitive to differences between the observed and predicted means as well as to certain changes in proportionality (Willmott, 1981). Note that analogously to r, d is measured from 0 to 1, 1 denoting maximum agreement.

2.4. Observations

For validation purposes, oceanographic and coastal meteorological measurements from the Spanish Harbour Agency (Puertos del Estado, http://www.puertos.es) are used. Specifically, data obtained from a tide gauge, a coastal wave buoy, a deep water buoy, and an HF radar (see Figure 2).

The tide gauge (B1) is located at 41.08°N, 1.21°E and was deployed in May 2011. For the study period, B1 had 98% data availability. The deep water buoy (B2) was deployed in August 2004 and corresponds to an ocean Seawatch buoy located at 40.68°N, 1.47°E at 688 m depth. This buoy measures water velocity and water temperature at the subsurface (nominal depth of 3 m) and wind vectors at 3 m above the sea surface, among other parameters. In this case, data availability reaches 99%. The coastal wave buoy (B3), located at 41.07°N, 1.19°E at 15 m depth and deployed in November 1992, is a directional wave buoy that includes a temperature sensor. The data availability for this instrument during the study period is 96%.

The HF radar system became operational in December 2013 and consists of three remote shelf-based sites. Each site comprises a transmitter-receiver antenna operating at a nominal frequency of 13.5 MHz with a 90 KHz bandwidth. The system provides hourly measurements of the current velocities in the first upper meter of the water column with a horizontal resolution of 3 km and a cutoff filter of 100 cm/s. See Lorente et al. (2015) for further information about the system.

HF radar measurements are subject to many potential errors (Graber & Haus, 1997). With the aim of minimizing them, an analysis of the data availability is carried out in order to reject low-confidence measuring points. Figure 2a shows that the central area of the radar domain has more than 80% data available, but near the boundary there are points with lower data availability (in some cases less than 10%). Following the criteria used by Lorente et al. (2015), only the HF radar points with more than 50% of data availability are used in the validation. The resulting validation area is shown in Figure 2b, which also shows the location of the tide gauge and the buoys, as well as the points used for validation and analysis of the model results.

Table 1
Along- (u) and Cross-Shelf (v) Current Components Statistics From the Comparison Between the Available HF Radar Data and the Available Buoy Data (B2) for the Study Period

	Bias (cm/s)	RMSD (cm/s)	*r*	*d*
Along-shelf component	1.18	7.52	0.76	0.86
Cross-shelf component	0.02	6.48	0.82	0.90

The comparison between HF radar and subsurface water currents measured in B2 shows good agreement for both along- and cross-shelf components. Some statistical values are presented in Table 1. The RMSD and *r* values are 7.52–6.48 and 0.76–0.82, respectively, which are within the ranges found by Lorente et al. (2015).

2.5. Numerical Model Analysis Methods

The first way of showing the results is by means of figures and their visual interpretation. Then, some aspects are analyzed in more detail. In this section, the methods used to analyze the model output are presented.

The buoyancy or Brunt-Väisälä frequency (N) is used to study the vertical structure of the water column.

$$N=\sqrt{-\frac{g}{\rho_0}\frac{\partial\rho(z)}{\partial z}} \tag{5}$$

where ρ_0 is the reference density and g is the gravitational acceleration.

When studying the surface mixed layer (SML) depth, Lentz (1992) established that it is proportional to wind stress, inversely proportional to vertical temperature gradient and independent of surface heat flux. The author also showed that the SML depth can be characterized by means of the parametrization (Pollard et al., 1972; Weatherly & Martin, 1978)

$$\delta=Au^*\frac{1}{\sqrt{Nf}} \tag{6}$$

where $u^*=\sqrt{\tau_s/\rho_0}$ is the shear velocity, τ_s is the wind stress magnitude, N is the buoyancy frequency just below the SML, f is the Coriolis frequency, and A is a proportionality constant. In this manuscript, this parametrization is used with the aim of evaluating the stratification and wind stress effect on the SML depth.

The "international one-atmosphere equation of state of seawater" (Millero & Poisson, 1981) is used to study the contribution of temperature and salinity to the density of the water column. The equation is of the form:

$$\rho=\rho_w+AS+BS^{1.5}+CS^2 \tag{7}$$

where S is the water salinity and ρ_w is the water density

$$\begin{aligned}\rho_w=&999.842594+6.793952\times10^{-2}t-9.095290\times10^{-3}t^2+1.001685\times10^{-4}t^3\\&-1.120083\times10^{-6}t^4+6.536336\times10^{-9}t^5\end{aligned} \tag{8}$$

and

$$A=8.24493\times10^{-1}-4.0899\times10^{-3}t+7.6438\times10^{-5}t^2-8.2467\times10^{-7}t^3+5.3875\times10^{-9}t^4$$

$$B=-5.72466\times10^{-3}+1.0227\times10^{-4}t-1.6546\times10^{-6}t^2$$

$$C=4.8314e-4$$

where t is the water temperature.

Several authors have used the momentum balance analysis to investigate the circulation over the continental shelf (Fewings & Lentz, 2010; Grifoll et al., 2016a; Lee et al., 1984; Lentz et al., 1999; Liu & Weisberg, 2005). In the present study, in order to analyze the mechanism that governs the circulation, an estimation of the size of the momentum balance terms is carried out. To do so, the cross-shelf (y axis) depth-integrated shallow-water equation is used:

$$\underbrace{\frac{\partial\overline{v}}{\partial t}}_{\text{acceleration}}+\underbrace{\frac{\partial\overline{uv}}{\partial x}+\frac{\partial\overline{v}^2}{\partial y}}_{\text{advection}}+\underbrace{f\overline{u}}_{\text{coriolis}}=-\underbrace{\frac{1}{\rho_0}\frac{\partial\overline{p}}{\partial y}}_{\text{pressure gradient}}+\underbrace{\frac{\tau_s^y}{H\rho_0}}_{\text{wind stress}}-\underbrace{\frac{\tau_b^y}{H\rho_0}}_{\text{bottom stress}} \tag{9}$$

where $H=\zeta+h$ is the total depth, ζ is the sea surface elevation, τ_s is the wind stress, τ_b is the bottom stress, and the overbar denotes a depth averaging:

$$(\bar{k}) = \frac{1}{H}\int_{-h}^{\zeta} k dz \tag{10}$$

where k is an arbitrary variable. The pressure gradient term includes the barotropic term (contribution of the sea level slope) and the baroclinic term (density contribution to the depth-averaged pressure gradient):

$$-\frac{1}{\rho_0}\frac{\partial \overline{p}}{\partial y} = -g\frac{\partial \zeta}{\partial y} - \frac{g}{H\rho_0}\int_{-h}^{\zeta}\int_{z'}^{\zeta}\frac{\partial \rho}{\partial y} dz' dz \tag{11}$$

3. Results

3.1. Wind Forcing and Wind-Jet Episodes Description

First, a comparison between the wind field from the WRF model and the observational data from B2 for the cross-shelf component is presented in Figure 3a. The numerical time series agree with the observed ones with a bias of −0.36 m/s, an RMSD of 2.62 m/s, an r of 0.77, and a d of 0.87 for the cross-shelf component. For the along-shelf wind component (not shown), similar values are obtained for the above mentioned metrics: 0.32 m/s, 2.26 m/s, 0.78, and 0.88, respectively.

Wind data show a larger percentage of NW winds from March to May and, uncommonly, also in July. The monthly maximum wind intensities are found in NW winds. The wind-jet events (intense wind from the NW) that exhibit a wind intensity of more than 10 m/s during at least 6 h are marked with green boxes in Figure 3. In total, nine episodes are selected (from E1 to E9). Table 2 shows the main characteristics of the selected events at V3, which is approximately located in the wind-jet axis, and some statistics comparing the WRF model data with buoy B2. Mean and maximum values show that during the warmer months, the intensities are lower than during the colder months, which is consistent with previous investigations (Grifoll

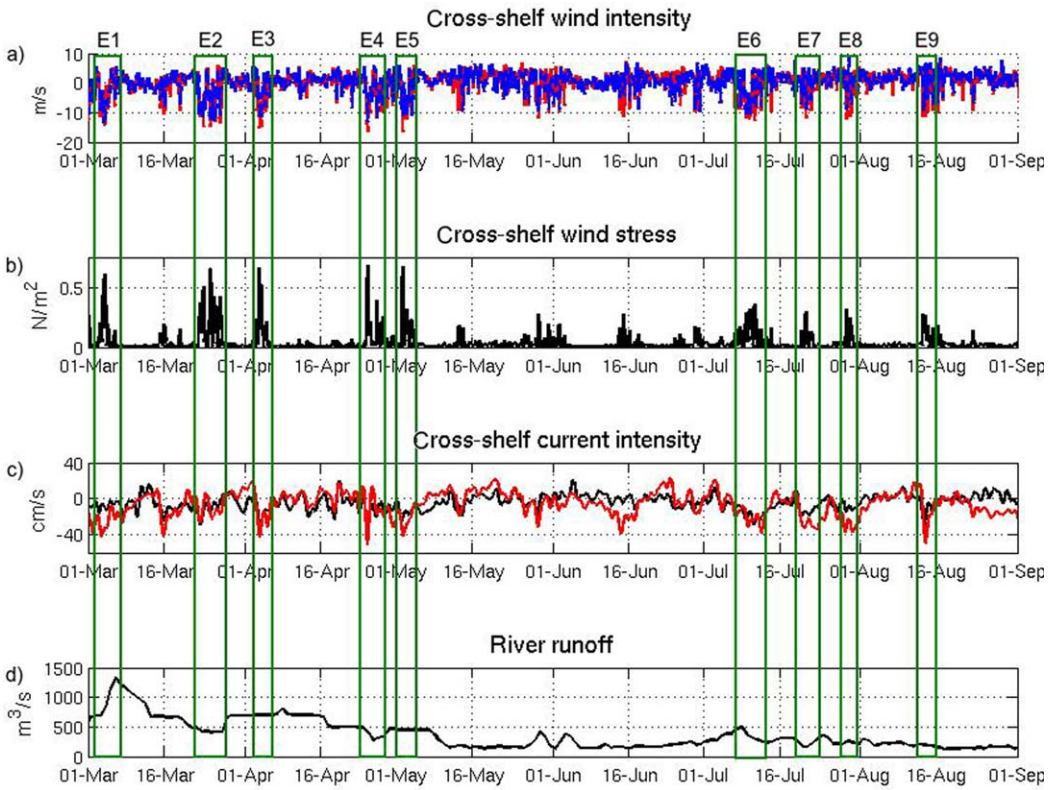

Figure 3. (a) Cross-shelf wind intensity comparison. In blue, data from buoy B2; and in red, data from the WRF model. (b) Numerical model cross-shelf wind stress at V3. (c) Filtered cross-shelf current intensity comparison. In black, data from the HF radar; and in red, the numerical model output. (d) Ebro River runoff. The green boxes represent the selected NW wind-jet events. The positive/negative values are according to the axis presented in Figure 2.

Table 2
Main Characteristics of the Wind-Jet Events at Point V3 (According to WRF Model Results) and Results of Bias and RMSD Between the WRF Model and B2 Wind Intensity

	Period (dd/mm/14)		Duration	Maximum	Mean		
	Start day	End day	(∼days)	intensity (m/s)	intensity (m/s)	Bias (m/s)	RMSD (m/s)
E1	03/03	05/03	2.0	17.11	10.81	0.24	2.66
E2	22/03	27/03	4.5	16.70	9.43	−0.67	2.45
E3	03/04	04/04	1.5	16.62	11.27	1.89	2.82
E4	25/04	26/04	1.0	17.03	11.69	0.62	1.60
E5	02/05	03/05	1.5	16.62	10.87	−0.29	1.97
E6	09/07	11/07	2.5	13.98	10.07	−0.62	2.17
E7	20/07	21/07	0.75	11.94	8.59	1.60	2.14
E8	29/07	30/07	1.3	11.88	8.33	−0.02	2.54
E9	13/08	14/08	1.25	11.68	9.42	1.55	2.68

Note. A negative (positive) bias means that the WRF model underestimates (overestimates).

et al., 2016b). The statistics show that the WRF model is able to capture the wind intensity during the wind-jet episodes fairly well, with biases that usually do not reach 1 m/s and RMSD values around 2 m/s. However, it should be noted that this point validation is done at B2, which is out of the wind-jet axis. Most of the events have a duration between 1 and 2 days. It is important to point out that E2 is much longer than the other events because it is an event with three wind peaks. In contrast, event E7 is very short and it has been selected because the hours of wind over 10 m/s are exactly the minimum imposed for the selection. And event E8, although it shows a duration of 1.3 days, is an event of two wind peaks and the sum of both peaks reaches the minimum established hours to be selected.

3.2. Skill Assessment of the Numerical Model

The comparison between sea level observations at B1 and numerical model results reveals an RMSD of 4.48 cm, an *r* of up to 0.86 and a *d* of 0.92. The model is able to reproduce the sea level variations but does not improve the results of IBI-MFC (imposed as boundary conditions), whose error metrics are 4.40 cm, 0.86, and 0.93, for RMSD, *r* and *d*, respectively. A statistical comparison of the surface temperature between the numerical model results and the observations of the buoys B2 and B3 is presented in Table 3, yielding reasonable agreement between the time series.

Some point error metrics of the modeled currents compared with the HF radar data are summarized in Table 4. In general, reasonably good agreement is found at points from V1 to V4, with values of RMSD, *r*, and *d* of 12.51–19.70 cm/s, 0.49–0.68, and 0.65–0.76, respectively. The RMSD present relatively high values because the numerical model currents have higher intensities than the HF radar measured currents. These skill metrics are in accordance with values found in previous works when comparing HF radar measurements with numerical models (Port et al., 2011; O011ERLINK "file, 2015; Lorente et al., 2016a). In contrast, at V5, the model does not seem to reproduce the surface water circulation properly. An explanation for this behavior is provided in Appendix A, where a more extensive analysis about the numerical model skill is done.

In Figure 3c, the time series of the filtered surface cross-shelf current intensity from the HF radar and the numerical model are compared. The filtered currents have been calculated using a tenth order Butterworth filter with a cutoff period of 30 h. In general, the model is able to capture the current variability during the wind jets. However the modeled intensities are higher than the measured ones, especially during E1, E7, and E8. A visual comparison of the water circulation observed by the HF radar and that obtained by the model during event E4 is presented in Figures 4b and 4c. The numerical model is able to reproduce the current pattern measured by the HF radar, but the results show higher current intensities than the measured ones.

Table 3
Values of Bias (°C), RMSD (°C), r, and d for the Surface Temperature at B2 and B3

	Bias	RMSD	*r*	*d*
Model versus B2	0.30	1.83	0.93	0.96
Model versus B3	2.26	2.79	0.95	0.91

3.3. Wind-Jet Events Analysis

The E4 event is the one that presents a more homogeneous wind field and a clear rise and fall of wind intensity. For this reason, it has been selected as a representation episode

Table 4
Values of Bias (cm/s), RMSD (cm/s), r, and d for the Along- and Cross-Shelf Surface Current Time Series at Points V1, V2, V3, V4, and V5 Comparing the Model Results With the HF Radar Data

	Along-shelf current component				Cross-shelf current component			
	Bias	RMSD	*r*	*d*	Bias	RMSD	*r*	*d*
V1	9.13	17.06	0.68	0.76	0.55	12.51	0.50	0.71
V2	0.43	13.88	0.61	0.75	0.24	14.19	0.61	0.75
V3	−0.94	18.18	0.49	0.69	2.20	17.61	0.54	0.70
V4	1.89	19.70	0.50	0.65	3.81	17.42	0.59	0.71
V5	−0.01	20.62	0.23	0.49	7.77	22.89	0.35	0.53

Note. All the *r* values are significant at *p* value < 0.01.

to show a detailed analysis of the evolution of the dynamics caused by the wind jet. The wind jet starts on April 25 at 02:00 (GMT) and peaks at 06:00, with velocities up to 17 m/s. The sequence is shown in Figure 4, where the columns correspond to four instants of the wind-jet evolution: before the wind jet starts, during the wind-jet increase, the wind-jet peak and the wind-jet decay. Throughout the wind-jet intensification, the surface currents (Figure 4c) intensify according to the increase of the wind intensity (Figure 4a) and the flow direction is consistent with the wind. When the wind stress decreases, the surface circulation turns parallel to the coastline, i.e., southwestward, perpendicular to the wind stress. The modeled sea level also presents a consistent sequence with the wind-jet evolution. Figure 4d shows the sea level obtained with the numerical model. During the wind-jet peak, a sea level set-down occurs near the coastline as a response to the wind stress.

Figure 5 shows the along- and cross-shelf wind stress components and subinertial water current at points A1 (11.3 m water depth) and V3 (76.1 m water depth) throughout the wind jet. The subinertial currents have been calculated using the filter mentioned in section 3.2. Near the coast (A1), before and after the wind jet, the along-shelf circulation prevails and a northeastward flow is observed. During the wind jet, the along-shelf component becomes less important. In contrast, in deeper regions (V3), the along-shelf flow during the wind jet is intensified and exhibits a southwestwardly flow. The cross-shelf circulation show a well-defined two-layer structure in both shallow and deep waters. This two-layer structure is characterized by a surface circulation that flows offshore and an onshore flowing circulation just below it. In deeper regions (V3), the two-layer structure has a return flow below the surface with much smaller intensities than that at the surface. Note that after the wind jet, when an inertial circulation emerges, the two-layer structure gradually disappears but, in deeper regions, the along-shelf subinertial surface circulation keeps flowing southwestward.

Figure 6 presents the evolution of the density anomaly obtained with the numerical model at the same instants as Figure 4. The results present an increase of the surface density (Figure 6a), which is displaced southwestward, likely due to the advection. In order to analyze the vertical structure, two vertical sections of the density anomaly are used: one following the axis of the wind jet (section A, Figure 6b) and one perpendicular to the wind jet (section B, Figure 6c). These vertical profiles show that before the wind jet starts, the water column is stratified and that during the wind jet the stratification decreases and the water column tends to homogenize. This stratification breakdown is more pronounced in the axis of the wind jet. However, from visual inspection, it is not possible to clearly discern if the homogenization process is due to upwelling/downwelling or a mixing process that cools the water surface. Looking at the temperature and salinity distributions and the vertical velocity profiles at the vertical section B (not shown), it is observed that during the wind jet the water at the surface becomes cooler due to a mixing process and, when the wind jet intensity diminishes, there appears a downwelling region at the west of the wind-jet axis, associated with a downward movement of the lighter and warmer surface waters. In contrast, at section A there is a clear upwelling region near the coast until approximately 45 m depth (4 km from the coastline), where the surface water temperature becomes equal to the bottom water temperature. Then, moving offshoreward, the water column likely starts to mix. Besides, it is important to note that there is an advection of the surface temperature that also contributes to the changes in the temperature field.

In order to extend the wind-jet response pattern in the vertical column during other episodes, the evolution of the buoyancy or Brunt-Väisälä frequency (N) is investigated. Figure 7 shows the Brunt-Väisälä frequency

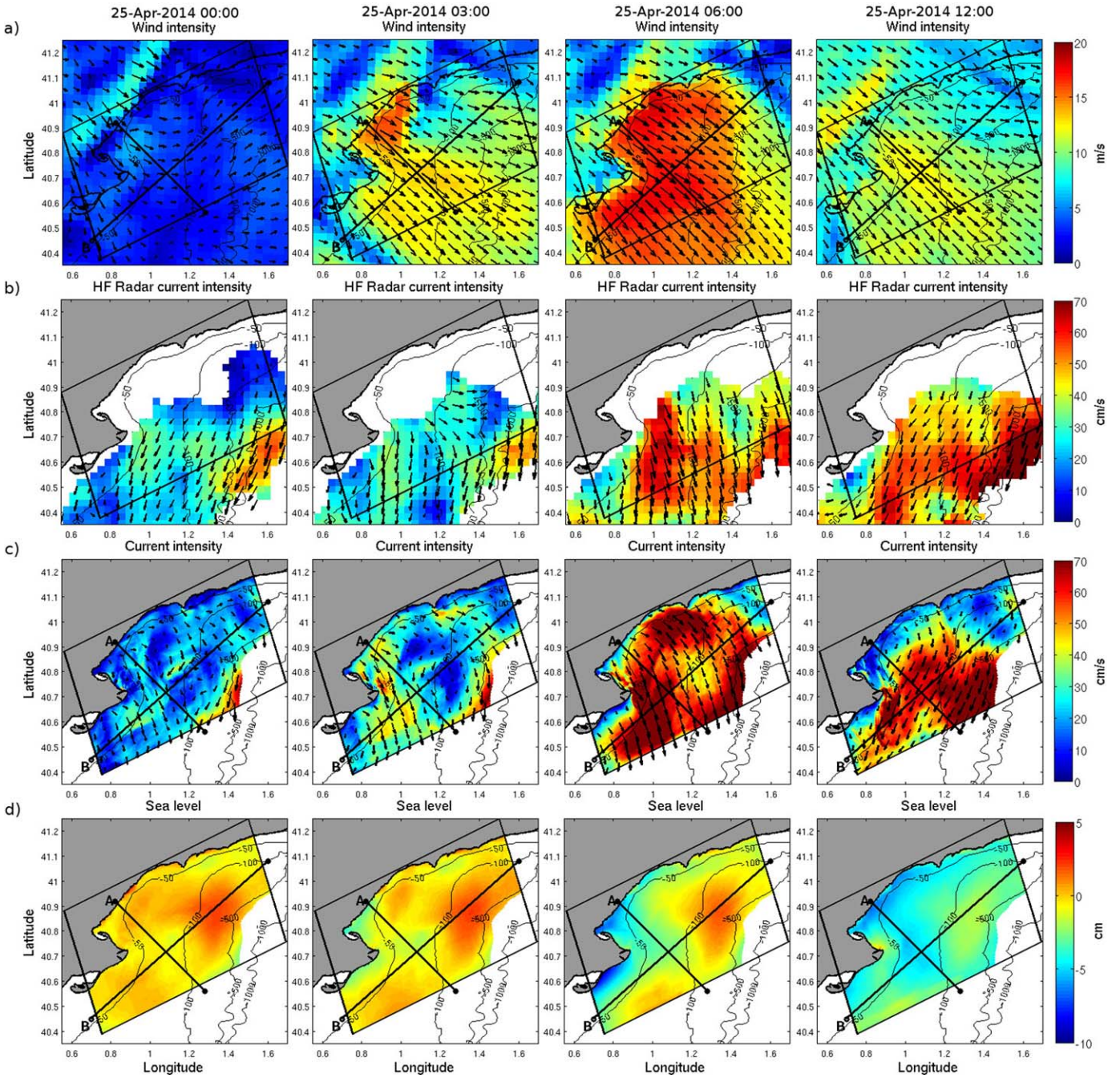

Figure 4. Results for the wind-jet event E4. (a) Wind intensity; (b) HF radar current intensity; (c) modeled current intensity; (d) modeled nontidal sea level. For clarity, the results are shown up to the mid-slope (i.e., 600 m depth).

evolution (before and after the wind jet) for the episodes selected in section 3.1. The selected point is V4, which is far enough to avoid the river plume interference and, therefore, allows a clearer visualization of the results. Different patterns are observed according to the evolution of *N*. During colder episodes (i.e., E1, E2, E3, which occurred during March and early April), the water column becomes homogenized after the wind jet. In these cases, the wind stress momentum transfer is able to reduce the stratification, resulting in a well-mixed water column, i.e., there are weak vertical gradients. In contrast, during warmer episodes, where the water column is more stratified, the wind-induced mixing is not able to homogenize the whole water column and only a deepening of the pycnocline is observed after the wind jet.

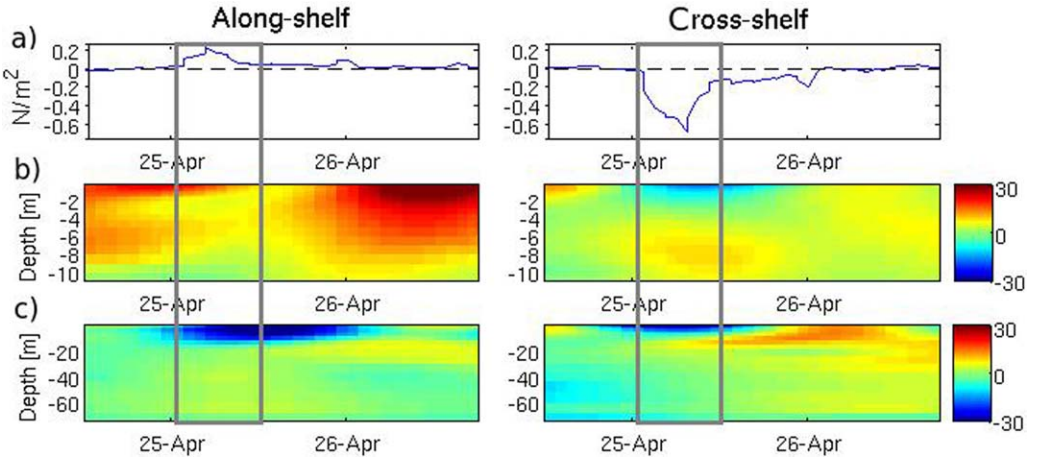

Figure 5. (left) Along-shelf and (right) cross-shelf components of (a) wind stress, (b) subinertial water velocity at A1, and (c) subinertial water velocity at V3.

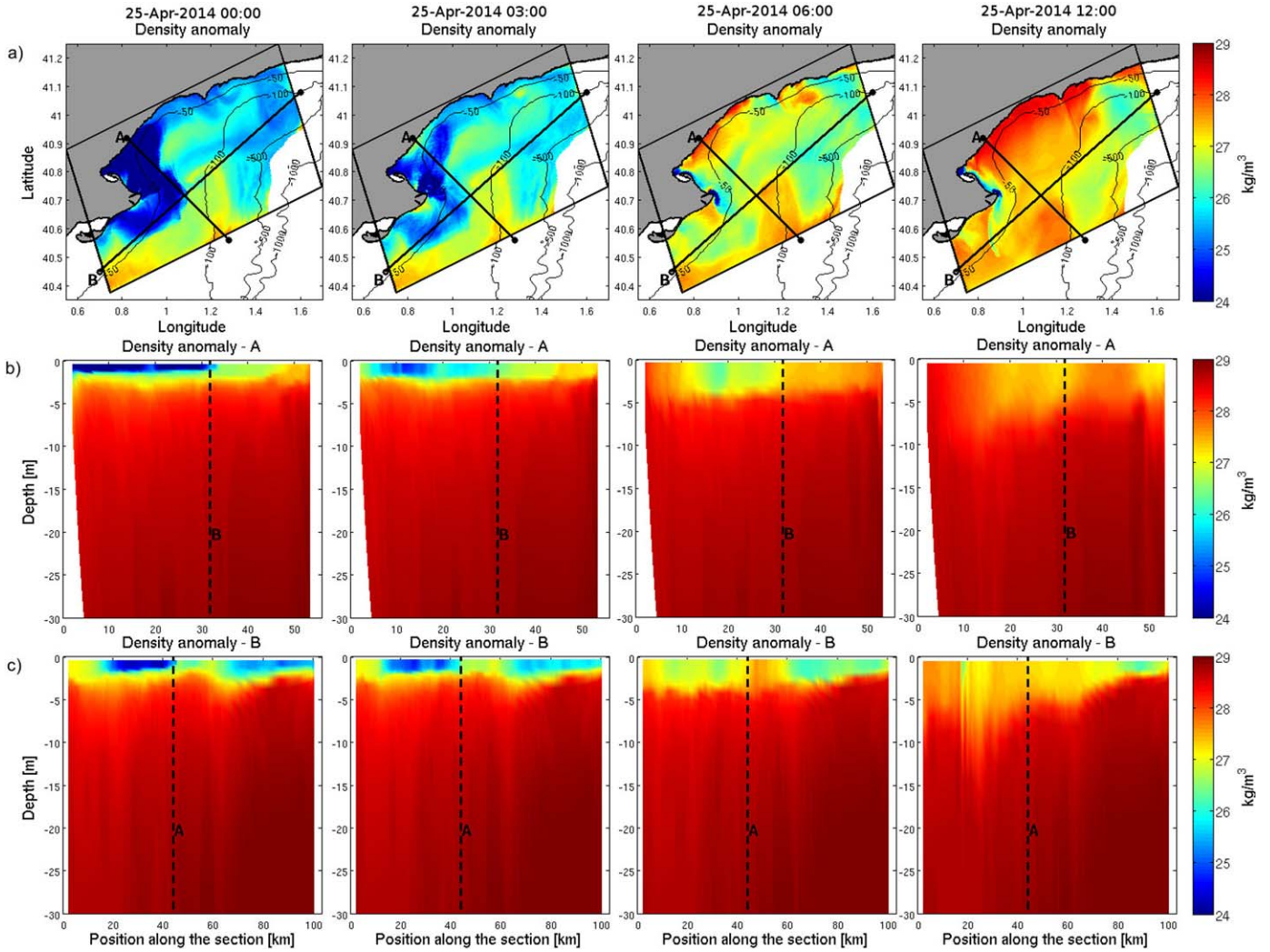

Figure 6. Model results of density anomaly during the wind-jet event E4. (a) Results at the surface, (b) a vertical profile of section A, and (c) a vertical profile of section B. For clarity, the results are shown up to the mid-slope (i.e., 600 m) in Figure 6a, and up to −30 m in Figures 6b and 6c.

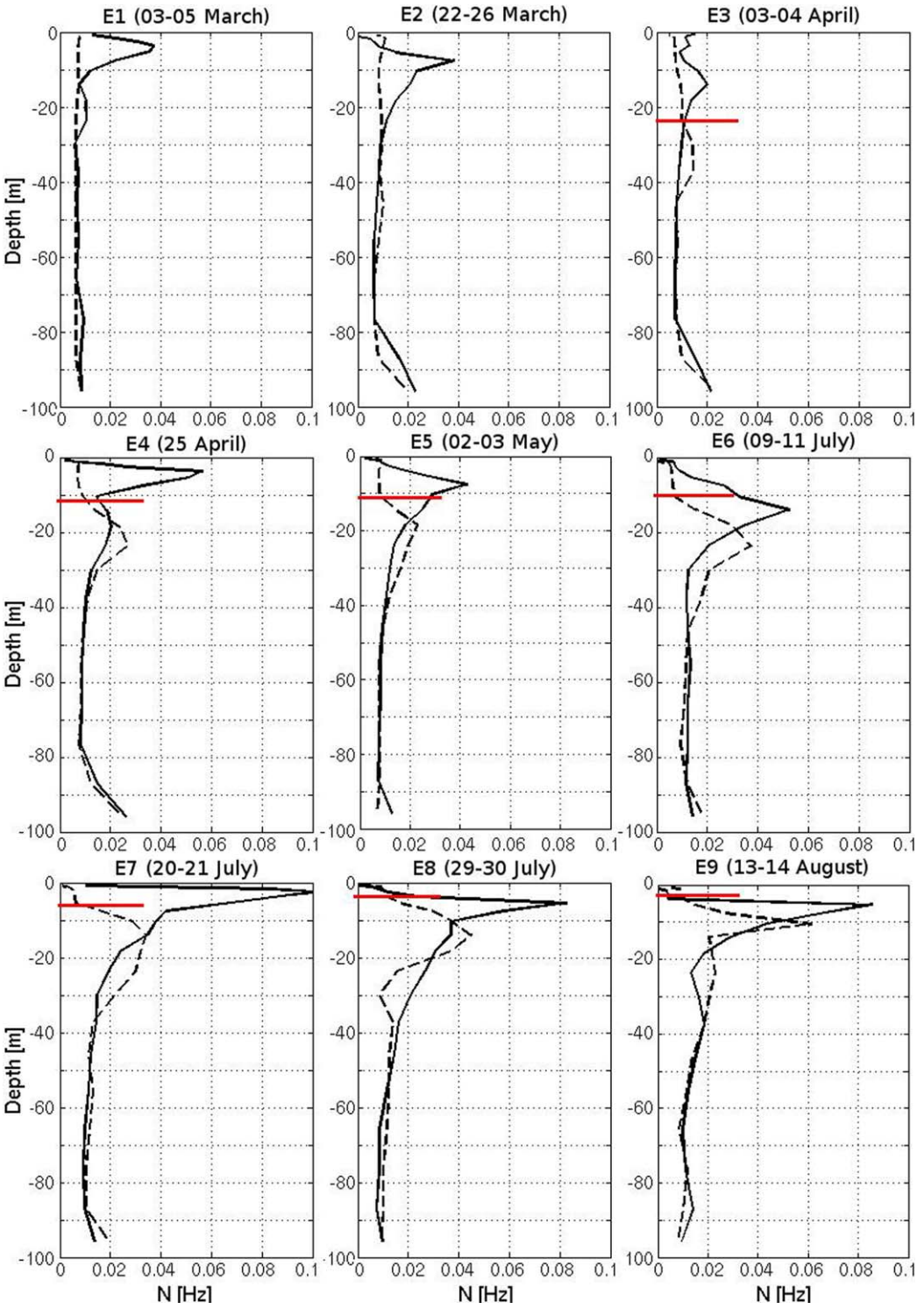

Figure 7. Evolution of the Brunt-Väisälä frequency at the start of the wind jet (solid line) and at the end of it (dashed line) at point V4 for all wind-jet episodes (E1–E9). The red lines are the SML depths.

In Figure 7, it is also observed a reduction of the wind-induced mixing when moving toward warmer months (e.g., E9, which corresponds to August): the resulting SML depth (i.e., the distance between the surface and the top of the pycnocline) becomes thinner after the wind jet. In events E1 and E2, the whole water column becomes mixed, in E3 the SML depth is around 24 m, in E4 is 12 m, in E5 11 m, in E6 is 10 m,

and from E7 to E9 the SML depth is less than 10 m. These results can be explained looking equation (6), where the SML depth increase linearly with u^* and decrease exponentially with N. Thus, the smaller the N is (less stratified), the higher the SML depth becomes.

In order to determine which is the main contributor to water column stratification, the temperature and salinity vertical profiles have been calculated using equation (7). The temperature (salinity) contribution to density is calculated assuming constant salinity (temperature). The comparison of these profiles with the density profile (not shown) for all events shows a clear change of the density profile due to a change in temperature (the salinity contribution is almost invariant) except in E1, where salinity plays an important role due to high river runoff, which reaches values of 1,300 m^3/s (see Figure 3). The fact of having a change in density due to a change in temperature and an unaltered salinity, indicates that the water column in this point is under a mixing process.

The numerical results show a similar flow structure in all selected events, where a two-layer flow is always originated. Figure 8 presents the wind intensity and the current vertical profile along section A for two events: E4 (less stratified and higher wind intensity) and E9 (more stratified and weaker wind intensity). During E4, the two-layer structure occupies the whole water column (the onshore return flow reaches the bottom). In contrast, in event E9, the two-layer cross-shelf circulation is clearly confined to the SBL (below that, where the return flow ends, the circulation is almost nonexistent). This indicates that the transition from inner to mid-shelf occurs in shallower waters. During less stratified events (e.g., E4), the SBL intersects the bottom in almost the whole domain (most of the section is at the inner shelf), while in more stratified events (e.g., E9) the SBL is thinner, and thus, the intersection with the bottom is reduced, i.e., the inner shelf is narrower, and most of the transversal section is in the mid-shelf.

Figure 8 also shows the influence of the spatially varying wind stress. During E4, when a relatively homogeneous wind field occurred, the first zero-crossing depth (from offshore to onshore flow) is almost uniform along the transect. However, during E9, where the wind along section A is not homogeneous, this first zero-

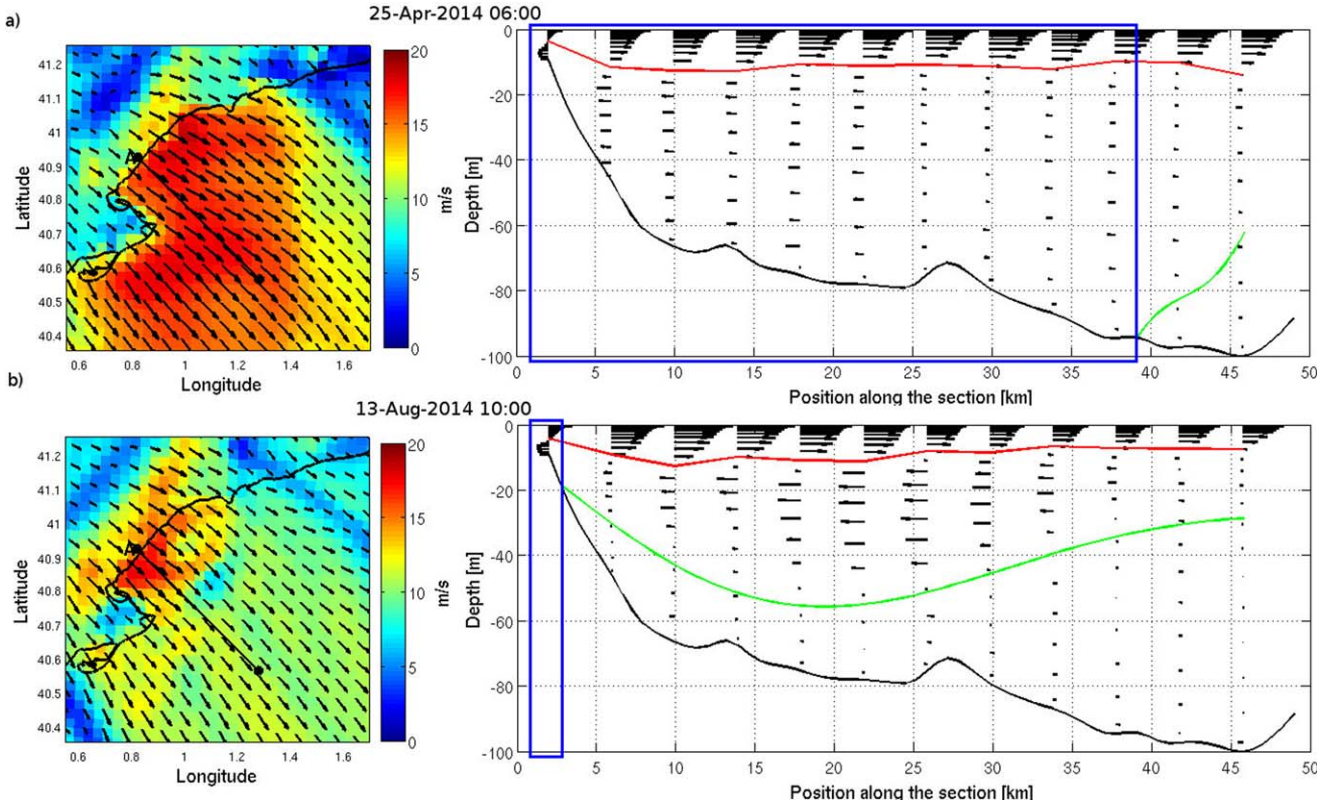

Figure 8. (left) Wind intensity and (right) water velocity profile during (top) E4 and (bottom) E9. The vectors of the vertical profile are plotted every six points. The red line is the first zero-crossing (related to the SML depth), the green line is the SBL depth, and the blue box delimits the inner shelf region.

Table 5
Estimated Mean and Standard Deviation of the Cross-Shelf Momentum Balance Terms During a Period of 12 h (Units Are $m/s^2 \times 10^{-6}$) in A1 (∼11 m Depth), A2 (∼47 m Depth), V3 (∼76 m Depth), and V4 (∼99 m Depth) for the Wind-Jet Event E4 and Before It

Cross-shelf		$\frac{\partial \overline{v}}{\partial t}$	$+\frac{\partial \overline{u}\,\overline{v}}{\partial x}$	$+\frac{\partial \overline{v}^2}{\partial y}$	$+f\overline{u}$	=	$-\frac{1}{\rho_0}\frac{\partial \overline{p}}{\partial y}$	$+\frac{\tau_s^y}{H\rho_0}$	$-\frac{\tau_b^y}{H\rho_0}$
A1	Before E4	−0.26	1.48	−2.42	2.86		1.56	0.22	−0.12
		±1.16	±0.60	±0.74	±1.22		±1.09	±0.99	±0.84
	E4	−1.00	0.40	−8.03	5.17		30.31	−28.80	−4.97
		±1.61	±2.91	±2.56	±3.52		±14.98	±18.60	±3.34
A2	Before E4	0.35	−0.10	−1.03	6.64		5.97	0.08	−0.20
		±0.39	±0.95	±0.73	±0.33		±0.64	±0.31	±0.16
	E4	−1.49	−0.18	−3.53	2.58		5.73	−8.06	−0.29
		±0.71	±0.99	±4.47	±2.62		±4.06	±5.52	±0.19
V3	Before E4	−0.56	−1.30	2.70	−2.69		−2.48	0.04	0.59
		±1.00	±0.37	±0.76	±0.85		±1.38	±0.04	±0.16
	E4	0.30	0.29	−0.07	−1.37		3.15	−4.21	0.22
		±1.37	±0.55	±1.62	±1.36		±3.33	±2.71	±0.19
V4	Before E4	−0.22	−0.14	0.53	−2.18		−2.14	0.03	0.09
		±0.43	±0.25	±0.23	±0.79		±0.59	±0.05	±0.05
	E4	−0.79	−0.21	−0.18	−1.47		−0.08	−2.65	0.08
		± 1.15	±0.47	±0.78	±0.58		±1.96	±1.88	±0.06

crossing depth is not constant. In this case, when the wind intensity decreases, the upper part of the SBL (where the flow is offshore-ward) is reduced and the SBL becomes smaller.

The results of the cross-shelf momentum balance are presented in Table 5. In order to evaluate the relevance of each term, the mean and the standard deviation computed over a period of 12 h are provided. The results are presented at four different points, A1, A2, V3, and V4 (from shallower to deeper waters), and for two different periods: throughout the calm before E4 and during the wind-jet event E4.

During the calm period, the flow tends to be geostrophic in the cross-shelf component, with a momentum balance between the Coriolis force and the pressure gradient terms. In some cases, the nonlinear terms are also important. This is because during a calm period the along-shelf circulation may become important and, at shallow regions, the bathymetric features can also play an important role.

In the course of the wind jet, the relative importance of the dominant terms in the momentum balance is modified. From A2 to V4, the momentum balance shows a balance between the wind stress, the pressure gradient and the Coriolis force term (associated with the wind-driven along-shelf transport). However, the relative importance of the pressure gradient term tends to diminish moving offshore (to deeper waters). This seems to indicate that there is a transition zone toward a balance between the wind stress and the Coriolis force terms, characterizing a transition to the mid-shelf. Then, in shallower waters (A1 and A2), there is an increase of the relative importance of the nonlinear terms and, in A1, the bottom stress term also increases. Nevertheless, at A1 the main momentum terms are the pressure gradient and the wind stress. This is due to the sea level set-down observed in our results, and consistent with the results presented in Fewings and Lentz (2010) and Lentz and Fewings (2012), since an offshore-ward wind stress balances the cross-shelf pressure gradient with a sea level set-down.

In order to inspect the momentum balance of all the wind-jet events, a ternary plot of the surface stress, pressure gradient and Coriolis terms is shown in Figure 9. This ternary plot has been done adding the three terms and calculating the proportion of each one for every wind-jet event at three different locations: A1, V4, and A7. At the shallowest point in the wind-jet axis (A1), all the events present a balance between the pressure gradient and the surface stress terms, with a very small contribution of the Coriolis term. Thus, A1 is in the inner shelf for all the events. Going to deeper waters (V4), different behaviors are observed depending on the different events. For event E3, point V4 is still in the inner shelf. For events E1 and E5, point V4 is in a transition zone. For events E2 and E4, the balance is mainly due to the surface stress and the Coriolis terms, thus the point is located at the mid-shelf. Finally, events E6, E7, E8, and E9 show a geostrophic

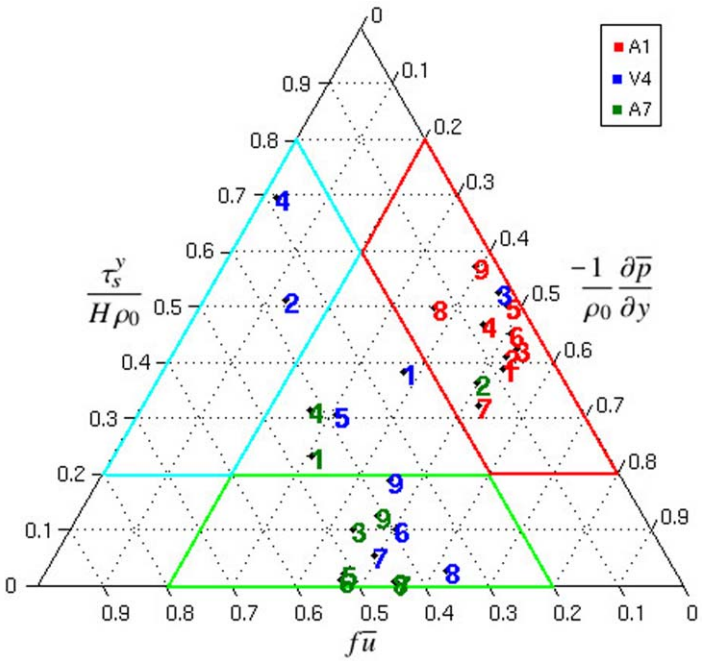

Figure 9. Ternary plot between the surface stress, pressure gradient, and Coriolis terms for each wind-jet event and at three different locations: A1 (red), V4 (blue), and A7 (green). The color boxes are the regions where the balance is mainly due to two of the three terms. The red box corresponds to a balance between the pressure gradient and the surface stress terms; the green box corresponds to a balance between the pressure gradient and the Coriolis terms; and the blue box corresponds to a balance between the surface stress and the Coriolis terms.

balance, indicating that the region is barely affected by the wind jet and that V4 is located in the outer-shelf. It should be noted that these events are the ones with less wind intensity. Now, looking for the behavior at a point out of the primary wind-jet axis, it is observed that at A7 most of the events present a geostrophic balance (the point is not affected by the wind jet). However, for events E1, E2, and E4, point A7 is affected by the wind jet. This is due to the wider wind field of these wind-jet episodes.

4. Discussion

4.1. Wind-Jet-Induced Dynamics

The theoretical shelf response to cross-shelf winds has been analyzed in previous research. Pond and Pickard (1983) explained that when the wind remains constant in direction but varies in speed, the Ekman transport perpendicular to the wind varies and the upper-layer waters are forced toward or away from each other, generating convergence or divergence. Then, for continuity, the convergence (divergence) is accompanied by a downward (upward) motion, namely downwelling (upwelling). Focusing at the Ebro Shelf, a theoretical shelf response was investigated by Jordà (2005) using numerical modeling under simplified conditions. The author found that during a stationary NW wind-jet episode, the water velocities perpendicular to the wind jet are larger in the axis of the wind jet than at the edges, resulting in a divergence zone in the east (associated with a decrease of surface elevation and an upwelling of denser waters) and a convergence zone in the west (associated with an increase of the surface elevation and a downwelling of lighter waters). The realistic simulations presented in this manuscript have allowed the authors to identify some of the characteristics mentioned above. The sea-surface elevation (see Figure 4d) exhibits a clear sea level set-down throughout the wind jet. Additionally, when the flow is perpendicular to the wind-jet axis, the sea level presents a decrease east of the wind-jet core and an increase to its west. Besides, a downwelling region is observed at the west of the wind-jet axis when the wind-jet intensity diminishes. During the wind jet, the along-shelf current velocity in deeper regions present a structure similar to the model suggested by Pond and Pickard (1983), with a divergence zone east of the wind-jet axis and convergence to its west. However, the transitory nature of the forcing mechanisms and the nonuniform bathymetry lead to complex behavior in the along-shelf direction dominated by along-shelf gradients. This probably explains the increase of the along-shelf flow shown after the wind-jet (Figure 5) related to the transient set-down near the coast. In this sense, Csanady (1980) showed that strong cross-shore wind can generate substantial along-shelf flow due to the presence of a trapped pressure field on the inner shelf.

The small upwelling region near the coastline found in our results is consistent with the theoretical study of Pond and Pickard (1983). In this case, when the wind causes the surface layer to move away from the coast but there is no supply of surface water (due to the coast), water from below the surface must rise to replace it. Additionally, this behavior is linked with the two-layer flow structure observed in our numerical results, where water from deeper layers must upwell near the coast to replace the water flowing offshore at the surface. The two-layer flow structure has been previously observed in the Ebro Shelf by Grifoll et al. (2015, 2016b) and is consistent with results of other investigations (Fewings et al., 2008; Grifoll et al., 2013; Horwitz & Lentz, 2014; Tilburg, 2003), where a two-layer flow structure due to cross-shelf winds has been found at the inner shelf. This two-layer behavior was first investigated by Ekman (1905), who analytically found the existence of an upper current in the direction of the wind and a compensating, comparatively weak current running in the opposite direction below.

Grifoll et al. (2015) used ADCP observations at the Ebro Shelf and observed that during stratified seasons, the intense cross-shelf winds resulted in a well-defined two-layer flow and were more effective at driving

offshore transport than during unstratified conditions, when a one-layer structure appeared. Nevertheless, Lentz and Fewings (2012) noted that the flow structure is similar for stratified and unstratified conditions. Previous studies about the influence of the stratification in the cross-shelf transport also exhibit differences. On the one hand, Fewings et al. (2008) noted that stratification suppresses vertical mixing and, therefore, the SBL is reduced, producing a stronger cross-shelf circulation and an onshore displacement of the boundary between the inner shelf and the mid-shelf. Also, Dzwonkowski et al. (2011) found that as stratification increases, the boundary layer extent is reduced and the transport fraction is enhanced. On the other hand, Tilburg (2003) posited that strong stratification or weak winds lead to shallower surface boundary layers and that strong stratification results in smaller upwelling/downwelling zones and a reduction of the cross-shelf transport.

Our numerical results have provided evidence of a complex response to a wind jet, where all events present a two-layer flow structure. In the episodes where the water is more stratified, there is a reduction of vertical mixing and thus, the SML is thinner (similar to Fewings et al., 2008). It has also been observed that when the water column is more stratified or the wind is less intense, the SBL is reduced, agreeing with previous investigations (Dzwonkowski et al., 2011; Fewings et al., 2008; Tilburg, 2003). This indicates that the transition from the inner shelf to the mid-shelf occurs in shallower waters, i.e., the inner shelf region is reduced, which is consistent with results from previous studies (Fewings et al., 2008; Lentz & Fewings, 2012). In order to discern if the differences are due to the different stratification conditions or due to the different wind intensities, a simple test is done. Using equation (6) the SML depth along section A is calculated for each event. Then, the effect of wind (stratification) is estimated considering the N (u^*) parameter constant (using as constant value the mean along the section). Finally, the regression slopes when comparing the "real" SML depth with both the SML depths calculated with constant u^* and with constant N have been calculated for each wind-jet event. The results show that for events E1 to E4, the regression slopes for the stratification effect have values ranging from 0.59 to 0.84, while the wind effect has values from 0.13 to 0.38. In contrast, the SML depth for events E5 to E9 show regression slopes from 0.10 to 0.45 for the stratification effect and values from 0.54 to 0.85 for the wind effect. A plausible explanation for these results is that for more stratified events, where the SML depth is smaller, the wind plays a more important role because the layer of water where it affects is smaller. And for the events less stratified, where the SML depth is higher, the wind effect is smaller because the water column where it affects is bigger and thus the stratification plays a more important role.

Regarding the cross-shelf momentum balance, Lentz et al. (1999) distinguished among regions with different dominant momentum balance terms on the North Carolina Shelf. At the inner shelf, the pressure gradient tended to be balanced by the frictional terms (wind and bottom stresses) and, at the mid-shelf, there was generally a geostrophic balance (i.e., a balance between the Coriolis force and the pressure gradient terms). However, the dynamics during a cross-shelf wind is different. In this sense, Lentz and Fewings (2012) distinguished between the inner and mid-shelf responses to a cross-shelf wind stress. They revealed that, at the inner shelf, the bottom stress reduces the along-shelf transport and a pressure gradient develops to partially balance the wind stress. In contrast, at the mid-shelf, the wind stress is balanced by the Coriolis force and there is no pressure gradient. In the present study, it has been found that, during a calm period the flow is geostrophic, as expected according to other research (e.g., Fewings & Lentz, 2010; Lentz et al., 1999; Liu & Weisberg, 2005). During the wind-jet events, a balance between the pressure gradient and the surface stress terms is observed at shallow waters, which is the typical behavior at the inner shelf. Then, moving to deeper regions, there is an increase of the relative importance of the Coriolis force term. In some events, the Coriolis force term balances with the surface stress term (i.e., the region is located at the mid-shelf), other events present a balance between the three terms (i.e., are in a transition zone) and other events are in geostrophic balance (i.e., not affected by the wind jet). Overall, the momentum balance observed in the results present similar patterns as the reported by Lentz et al. (1999) (during the calm period) and Lentz and Fewings (2012) (during the wind jet).

5. Conclusions

A numerical model at the north Ebro Shelf has been implemented, run for 6 months and validated, presenting good agreement with observational data. Within the studied period, nine wind-jet events have been

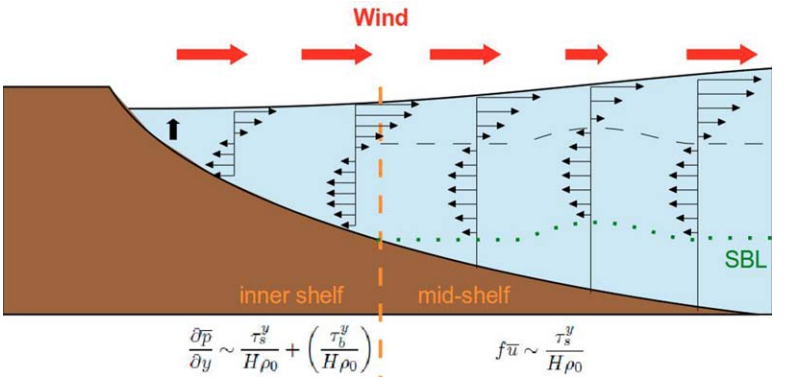

Figure 10. Schematic diagram of the cross-shelf response to a nonhomogeneous wind jet. The green dots represent the depth of the SBL and the orange dashed line is the transition from the inner shelf (where the SBL intersects the bottom) to the mid-shelf. This transition is displaced onshore when the stratification is higher. The SBL depths vary with the wind intensity. The vertical structure presents a two-layer flow with an upwelling region near the coast (black arrow). A sea level set-down occurs near the coastline. The cross-shelf dynamical balance at the inner shelf is between the pressure gradient and the wind stress term. At very shallow waters, the bottom stress term is also relevant. In contrast, at the mid-shelf, the balance is between the Coriolis and the wind stress terms.

selected to investigate the shelf response in terms of water circulation. According to the numerical results, the water circulation response to a wind jet in the NES presents noticeable spatial and temporal variability. A schematic diagram of the main results is presented in Figure 10. During the wind-jet events, the cross-shelf circulation at the wind-jet axis presents a well-defined two-layer structure (offshore flow at near-surface and onshore flow in deeper layers), which is accompanied by a decreasing of the sea level near the coast and the occurrence of upwelling near the coastline. The vertical structure of the water column highly depends on the wind stress and the water stratification. Numerical results show that increasing the stratification reduces the SML and the SBL, thus the inner shelf region is narrower. The buoyancy frequency analysis has revealed that, during colder episodes, the wind momentum transfer penetrates unto deeper layers and the whole water column becomes mixed after the wind jet. During the warmer episodes, the water column presents a stratification reduction but, due to its initially higher stratification, it remains stratified after the wind jet. Finally, the cross-shelf momentum balance results have allowed to discern between the different continental shelf regions. At the wind-jet axis, all the events exhibit a balance between the pressure gradient and the surface stress terms at shallow waters (indicating that the point is located at the inner shelf). At deeper waters, one event remains at the inner shelf, some events present a balance between the Coriolis force and the surface stress terms (indicating that the point is located at the mid-shelf), other events present a combined balance between the Coriolis, the surface stress and the pressure gradient terms (indicating that the region is in a transition zone) and others are not affected by the wind jet and show a geostrophic balance. The momentum balance at a point out of the wind-jet axis shows that most of the events are in geostrophic balance but some events are affected by the wind jet, due to a wider wind field that reaches the evaluation point.

Appendix A: Numerical Model Skill Assessment

A complete visualization of the surface current error metrics in the HF radar domain is presented in Figure A1. After computing the RMSD, *r* and *d* of the numerical model, a heterogeneous pattern is observed. The error metrics revealed good results at the continental shelf but show some discrepancies at the SE corner of the domain, where the depth is more than 1,000 m. Two plausible explanations are provided for this abnormal behavior. First, the numerical model is configured with 20 sigma levels, being the vertical representation of this area relatively poor. For instance, at V3 (located at the continental shelf), the maximum distance between vertical layers is 8 m and, in contrast, at V5 (located at the SE corner of the domain, at the continental slope) there are layers that are separated up to 60 m. Second, it coincides with the region where IBI-MFC presents a major discrepancy with the HF radar data (Lorente et al., 2016b); thus, the model results might be strongly influenced by the quality of the imposed open-boundary conditions. Nonetheless, the aim of this section is to verify the numerical model in shallow

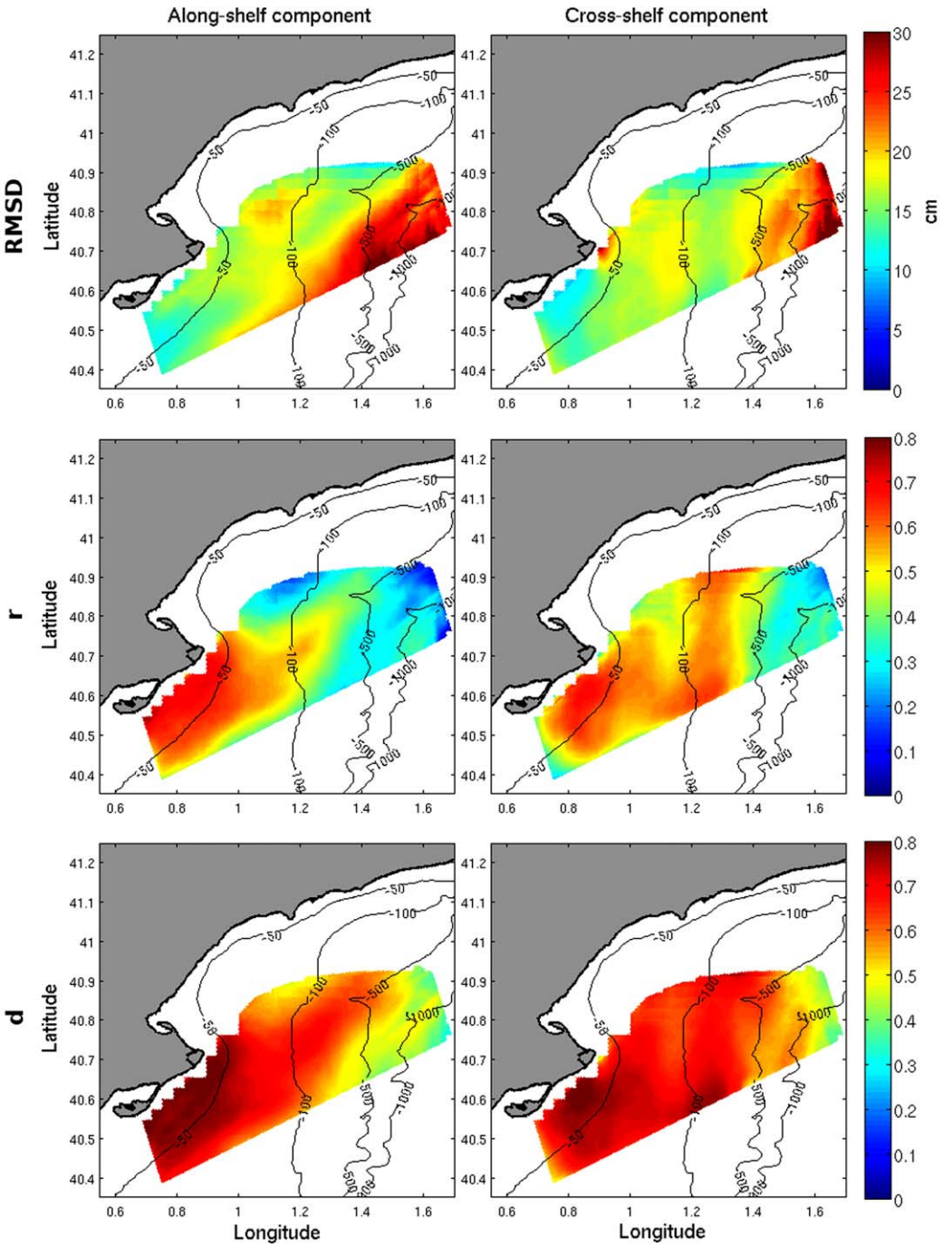

Figure A1. Statistical comparison between the numerically modeled currents and the HF radar data. Spatial variability of the (top) RMSD, (middle) *r*, and (bottom) *d* for the (left) along-shelf and (right) cross-shelf surface currents.

regions in order to study the wind-jet response at the continental shelf. For this reason, we exclude the lower right corner of the domain, which is outside of the continental shelf and where the results are not reliable. Finally it is worth noting that the HF radar estimations have an inherent uncertainty (see Table 1). For instance, considering the HF radar data as real for reference, the comparison between the HF data and our model provides a mean RMSD of around 15 cm/s, values of *r* between 0.4 and 0.7 and a mean *d* above 0.65, which reaches 0.8 at some points. The cross-shelf component shows better agreement with the HF radar data than the along-shelf component.

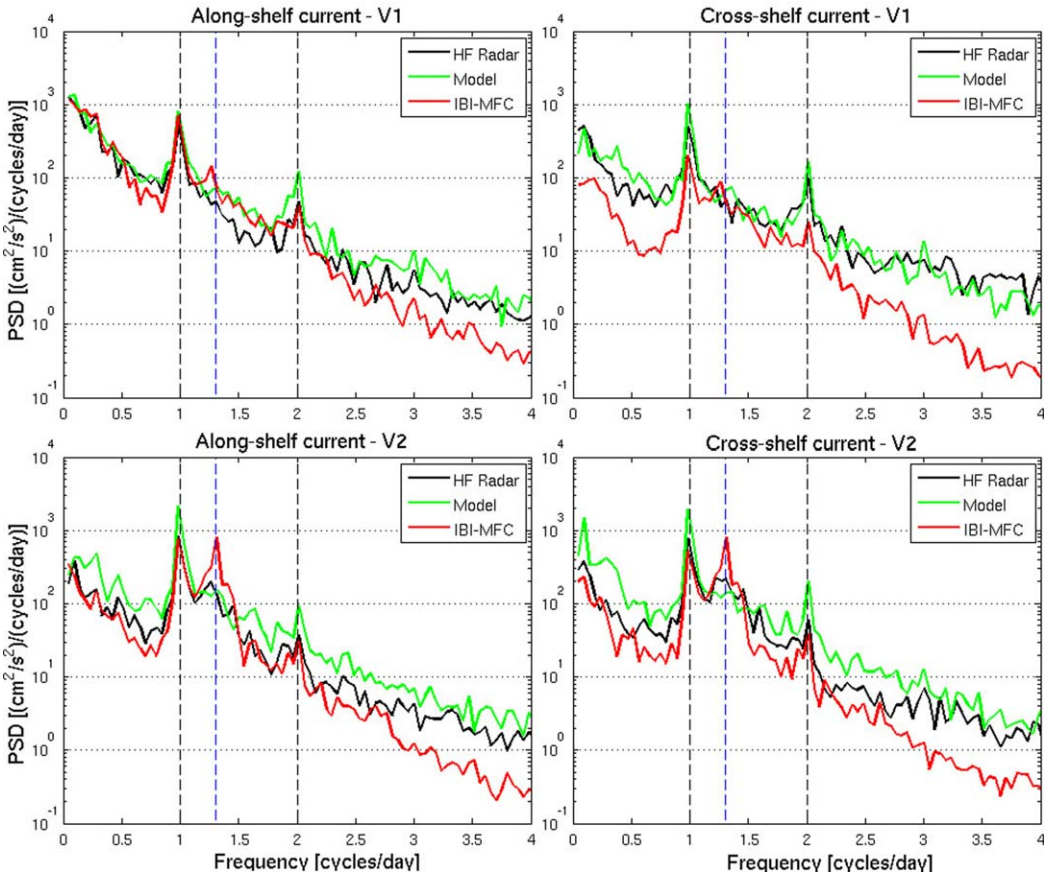

Figure A2. Power spectral densities of the (left) along-shelf and (right) cross-shelf surface current components at points V1 and V2. The HF radar data (black) is compared to the model results (green) and the IBI-MFC data (red). The dashed, vertical lines correspond to the inertial frequency (blue) and the diurnal and semidiurnal frequencies (black).

The energy spectra of the along- and cross-shelf surface current components (Figure A2) show that the dominant modes of temporal variability are within the diurnal and inertial frequencies. There is also a non-negligible peak at semidiurnal frequencies and an energetic band at low frequencies, while after 2 cycles per day (cpd) there is a sequentially drop of energy. Figure A2 shows that at V1 the model and the HF radar have a nonsignificant peak at the inertial frequency but IBI-MFC seems to indicate a small peak on the along-shelf component. Then, at V2, the inertial frequency increases in all cases. This behavior is expected, since at V1, which is at 13.3 m water depth, the frictional terms are expected to prevail and, at V2, at 62.2 m water depth, the frictional terms are less important. Another characteristic of the spectra is that the inertial frequency peak is higher at the points located at the center of the domain (not shown), revealing the prevalent clockwise motion in the area. In general, the IBI-MFC regional model tends to overestimate the inertial frequency in comparison to the HF radar data, while our coastal numerical model better reproduces the energy of this frequency. Also, at high frequencies, the model energy agrees better than IBI-MFC with the HF radar estimations. In contrast, the numerical model tends to overestimate the diurnal and semidiurnal peaks in comparison to the HF radar.

Acknowledgments
The development of this research is funded by the Doctorats Industrials 2013 PhD program (2013 DI 043) of the Catalan Government. L. Ràfols thanks the UPC (Universitat Politècnica de Catalunya) and the SMC (Servei Meteorològic de Catalunya) for their support. G. Jordà acknowledges a Ramón y Cajal program contract (RYC-2013–14714) funded by MINECO and the Regional Government of the Balearic Islands. The authors also acknowledge Puertos del Estado for the data set provided. This work has received funding from the UE H2020 program under grand agreement 730030 (CEASELESS project). HF radar data and buoy measurements used in this contribution can be consulted in http://portus.puertos.es, the IBI-MFC model data are available in http://marine.copernicus.eu, and the WRF model data were provided by the Catalan Service of Meteorology (http://meteo.cat/). The ROMS model output is available at 10.5281/zenodo.835498. Data processing and displaying was done using a licensed Matlab program.

References

Bolaños, R., Jorda, G., Cateura, J., Lopez, J., Puigdefabregas, J., Gomez, J., & Espino, M. (2009). The XIOM: 20 years of a regional coastal observatory in the Spanish Catalan coast. *Journal of Marine Systems*, *77*, 237–260. https://doi.org/10.1016/j.jmarsys.2007.12.018

Csanady, G. (1980). Longshore pressure gradients caused by offshore wind. *Journal of Geophysical Research*, *85*, 1076–1084.

Durand, N., Fiandrino, A., Frauni, P., Ouillon, S., Forget, P., & Naudin, J. (2002). Suspended matter dispersion in the Ebro ROFI: An integrated approach. *Continental Shelf Research*, *22*, 267–284. https://doi.org/10.1016/S0278-4343(01)00057-7

Dzwonkowski, B., Park, K., & Jiang, L. (2011). Subtidal across-shelf velocity structure and surface transport effectiveness on the Alabama shelf of the northeastern Gulf of Mexico. *Journal of Geophysical Research*, *116*, C10012. https://doi.org/10.1029/2011JC007188

Ekman, V. (1905). On the Influence of the Earth's Rotation on Ocean-Currents. *Arkiv for Matematik, Astronomi och Fysik*, *2*(11), 1–53.
Espino, M., Sánchez-Arcilla, A., & García, M. (1998). Wind-induced mesoscale circulation off the Ebro delta, NW Mediterranean: A numerical study. *Journal of Marine Systems*, *16*, 235–251.
Fairall, C., Bradley, E., Rogers, D., Edson, J., & Young, G. (1996). Bulk parameterization of air-sea fluxes for tropical ocean-global atmosphere Coupled-Ocean Atmosphere Response Experiment. *Journal of Geophysical Research*, *101*, 3747–3764.
Fewings, M., & Lentz, S. (2010). Momentum balances on the inner continental shelf at Martha's Vineyard Coastal Observatory. *Journal of Geophysical Research*, *115*, C12023. https://doi.org/10.1029/2009JC005578
Fewings, M., Lentz, S., & Fredericks, J. (2008). Observations of cross-shelf flow driven by cross-shelf winds on the inner continental shelf. *Journal of Physical Oceanography*, *38*, 2358–2378. https://doi.org/10.1175/2008JPO3990.1
Flexas, M., Durrieu de Madron, X., Garcia, M., Canals, M., & Arnau, P. (2002). Flow variability in the Gulf of Lions during the MATER HFF experiment (March-May 1997). *Journal of Marine Systems*, *33–34*, 197–214.
Font, J. (1986). *La circulación general a la mar catalana* (PhD thesis). Barcelona, Spain: Universitat de Barcelona.
Font, J., Garcia-Ladona, E., & Gorriz, E. (1995). The seasonality of mesoscale motion in the Northern Current of the western Mediterranean: Several years of evidence. *Oceanologia Acta*, *18*(2), 207–219.
Graber, H., & Haus, B. (1997). HF radar comparisons with moored estimates of current speed and direction: Expected differences and implications. *Journal of Geophysical Research*, *102*, 18749–18766.
Grifoll, M., Aretxabaleta, A., & Espino, M. (2015). Shelf response to intense offshore wind. *Journal of Geophysical Research: Oceans*, *120*, 6564–6580. https://doi.org/10.1002/2015JC010850
Grifoll, M., Aretxabaleta, A., Pelegrí, J., Espino, M., Warner, J., & Sánchez-Arcilla, A. (2013). Seasonal circulation over the Catalan inner-shelf (northwest Mediterranean Sea). *Journal of Geophysical Research: Oceans*, *118*, 5844–5857. https://doi.org/10.1002/jgrc.20403
Grifoll, M., Aretxabaleta, A., Pelegrí, J., & Espino, M. (2016a). Temporal evolution of the momentum balance terms and frictional adjustment observed over the inner shelf during a storm. *Ocean Science*, *12*, 137–151. https://doi.org/10.5194/os-12-137-2016
Grifoll, M., Navarro, J., Pallares, E., Ràfols, L., Espino, M., & Palomares, A. (2016b). Ocean-atmosphere-wave characterisation of a wind jet (Ebro Shelf, NW Mediterranean Sea). *Nonlinear Processes in Geophysics*, *23*, 143–158. https://doi.org/10.5194/npg-23-143-2016
Haidvogel, D., Arango, H., Budgell, W., Cornuelle, B., Curchitser, E., Lorenzo, E. D., . . . Wilkin, J. (2008). Ocean forecasting in terrain-following coordinates: Formulation and skill assessment of the Regional Ocean Modeling System. *Journal of Computational Physics*, *227*, 3595–3624.
Horwitz, R., & Lentz, S. (2014). Inner-shelf response to cross-shelf wind stress: The importance of the cross-shelf density gradient in an idealized numerical model and field observations. *Journal of Physical Oceanography*, *44*, 86–103. https://doi.org/10.1175/JPO-D-13-075.1
Jiang, H., Farrar, J., Beardsley, R., Chen, R., & Chen, C. (2009). Zonal surface wind jets across the Red Sea due to mountain gap forcing along both sides of the Red Sea. *Geophysical Research Letters*, *36*, L19605. https://doi.org/10.1029/2009GL040008
Jordà, G. (2005). *Towards data assimilation in the Catalan continental shelf* (PhD thesis). Barcelona, Spain: Universitat Politècnica de Catalunya.
Lee, T., Ho, W., Kourafalou, V., & Wang, J. (1984). Circulation on the continental shelf of the southeastern united states. Part I: Subtidal response to wind and gulf stream forcing during winter. *Journal of Physical Oceanography*, *14*, 1001–1012.
Lentz, S. (1992). The surface boundary layer in coastal upwelling regions. *Journal of Physical Oceanography*, *22*, 1517–1539.
Lentz, S., & Fewings, M. (2012). The wind- and wave-driven inner-shelf circulation. *Annual Review of Marine Science*, *4*, 317–343. https://doi.org/10.1146/annurev-marine-120709-142745
Lentz, S., Guza, R., Elgar, S., Feddersen, F., & Herbers, T. (1999). Momentum balances on the North Carolina Inner Shelf. *Journal of Geophysical Research*, *104*, 205–226.
Liu, Y., & Weisberg, R. (2005). Momentum balance diagnoses for the West Florida Shelf. *Continental Shelf Research*, *25*, 2054–2074. https://doi.org/10.1016/j.csr.2005.03.004
Lorente, P., Piedracoba, S., Sotillo, M., Aznar, R., Amo-Balandron, A., Pascual, A., . . . Alvarez-Fanjul, E. (2016a). Characterizing the surface circulation in Ebro Delta (NW Mediterranean) with HF radar and modeled current data. *Journal of Marine Systems*, *163*, 61–79. https://doi.org/10.1016/j.jmarsys.2016.07.001
Lorente, P., Piedracoba, S., Sotillo, M., Aznar, R., Amo-Balandron, A., Pascual, A., . . . Alvarez-Fanjul, E. (2016b). Ocean model skill assessment in the NW Mediterranean using multi-sensor data. *Journal of Operational Oceanography*, *9*, 75–92. https://doi.org/10.1080/1755876X.2016.1215224
Lorente, P., Piedracoba, S., Soto-Navarro, J., & Alvarez-Fanjul, E. (2015). Evaluating the surface circulation in the Ebro delta (northeastern Spain) with quality-controlled high-frequency radar measurements. *Ocean Science*, *11*, 921–935. https://doi.org/10.5194/os-11-921-2015
Mestres, M., Sierra, J., Sánchez-Arcilla, A., González del Río, J., Wolf, T., Rodríguez, A., & Ouillon, S. (2003). Modelling of the Ebro River plume. Validation with field observations. *Scientia Marina*, *67*(4), 379–391.
Millero, F., & Poisson, A. (1981). International one-atmosphere equation of state of seawater. *Deep-Sea Research Part A. Oceanographic Research Papers*, *28*(6), 625–629.
Millot, C. (1999). Circulation in the Western Mediterranean Sea. *Journal of Marine Systems*, *20*, 423–442.
O'Donncha, F., Hartnett, M., Nash, S., Ren, L., & Ragnoli, E. (2015). Characterizing observed circulation patterns within a bay using HF radar and numerical model simulations. *Journal of Marine Systems*, *142*, 96–110. https://doi.org/10.1016/j.jmarsys.2014.10.004
Pollard, R., Rhines, P., & Thompson, R. (1972). The deepening of the wind-mixed layer. *Geophysical Fluid Dynamics*, *4*(1), 381–404. https://doi.org/10.1080/03091927208236105
Pond, S., & Pickard, G. (1983). *Introductory dynamical oceanography*, 2nd ed. Oxford, UK: Butterworth-Heinemann.
Port, A., Gurgel, K., & Staneva, J. (2011). Tidal and wind-driven surface currents in the German bight: HFR observations versus model simulations. *Ocean Dynamics*, *61*, 1567–1585. https://doi.org/0.1007/s10236-011-0412-9
Riosalido, R., Vázquez, L., Gorgo, A., & Jansà, A. (1986). Cierzo: Northwesterly wind along the Ebro Valley as a meso-scale effect induced on the lee of the Pyrenees mountain range: A case study during ALPEX special observing period. *Scientific Results of the Alpine Experiment (ALPEX)*, *2*(108), 565–575.
Shchepetkin, A., & McWilliams, J. (2005). The regional oceanic modeling system (ROMS): A split-explicit, free-surface, topography-following-coordinate oceanic model. *Ocean Modelling*, *9*, 347–404.
Shimada, T., & Kawamura, H. (2006). Wind-wave developement under alternating wind jets and wakes induced by orographic effects. *Geophysical Research Letters*, *33*, L02602. https://doi.org/10.1029/2005GL025241
Skamarock, W. C., Klemp, J. B., Dudhia, J., Gill, D. O., Barker, D. M., Duda, M. G., . . . Powers, J. G. (2008). *A description of the advanceed research WRF, version 3* (NCAR Tech. Note NCAR/TN–475+STR). Boulder, CO: National Center for Atmospheric Research.

Tilburg, C. (2003). Across-shelf transport on a continental shelf: Do across-shelf winds matter? *Journal of Physical Oceanography*, *33*, 2675–2688.

Trasviña, A., Barton, E., Brown, J., Velez, H., Kosro, P., & Smith, R. (1995). Offshore wind forcing in the Gulf of Tehuantepec, Mexico: The asymmetric circulation. *Journal of Geophysical Research*, *100*, 20649–20663.

Weatherly, G., & Martin, P. (1978). On the structure and dynamics of the oceanic bottom boundary layer. *Journal of Physical Oceanography*, *8*, 557–570.

Willmott, C. (1981). On the validation of models. *Physical Geography*, *2*, 184–194.